Hydrogen, Oxygen, and Lead Adsorbates on Al 13 Co 4 (100): Accurate Potential Energy Surfaces at Low Computational Cost by Machine Learning and DFT-Based Data

Nathan Boulangeot, Florian Brix, Frédéric Sur, Émilie Gaudry

Hydrogen, Oxygen, and Lead Adsorbates on $Al_{13}Co_4(100)$: Accurate Potential Energy Surfaces at Low Computational Cost by Machine Learning and DFT-based Data

Nathan Boulangeot[*†], Florian Brix[*‡], Frédéric Sur[†], Émilie Gaudry[*§]

Abstract

Intermetallic compounds are promising materials in numerous fields, especially those involving surface interactions, such as catalysis. A key factor to investigate their surface properties lies in adsorption energy maps, typically built using first principles approaches. However, exploring the adsorption energy landscapes of intermetallic compounds can be cumbersome, usually requiring huge computational resources. In this work, we propose an efficient method to predict adsorption energies, based on a machine learning (ML) scheme fed by a few density functional theory (DFT) estimates performed on n sites selected through the Farthest Point Sampling (FPS) process. We detail its application on the $Al_{13}Co_4(100)$ quasicrystalline approximant surface for several atomic adsorbates (H, O and Pb). On this specific example, our approach is shown to outperform both simple interpolation strategies and the recent ML force field MACE [arXiv.2206.07697], especially when the number n is small, i.e., below 36 sites. The ground-truth DFT adsorption energies are much more correlated with the predicted FPS-ML estimates (Pearson R-factors of 0.71, 0.73, and 0.90 for H, O, and Pb, respectively, when n=36) than with interpolation-based or MACE-ML ones (Pearson R-factors of 0.43, 0.39, and 0.56 for H, O, and Pb, in the former case and 0.22, 0.35, and 0.63 in the latter case). The unbiased root mean square error (ubRMSE) is lower for FPS-ML than for interpolation-based and MACE-ML predictions (0.15, 0.17, and 0.17 eV, respectively, for hydrogen and 0.17 eV, 0.25 eV, and 0.22 eV for lead), except for oxygen (0.55, 0.47, and 0.46 eV) due to large surface relaxations in this case. We believe that these findings and the corresponding methodology can be extended to a wide range of systems, which will motivate the discovery of novel functional materials.

This is the author-manuscript version of

Nathan Boulangeot, Florian Brix, Frédéric Sur, Émilie Gaudry, Hydrogen, oxygen and lead adsorbates on $Al_{13}Co_4(100)$: accurate potential energy surfaces at low computational cost by machine learning and DFT-based data, *Journal of Chemical Theory and Computation*, vol. 20, no. 16, p. 7287-7299, 2024.

DOI: 10.1021/acs.jctc.4c00367

[*]Université de Lorraine, CNRS UMR7198, Institut Jean Lamour, Campus Artem, 2 allée André Guinier, 54000 Nancy, France

[†]Université de Lorraine, INRIA, CNRS UMR7503, Laboratoire lorrain de recherche en informatique et ses applications, Campus Scientifique, 615 rue du Jardin-Botanique, 54506 Vandœuvre-lès-Nancy, France

[‡]Center for Interstellar Catalysis, Department of Physics and Astronomy, Aarhus University, DK-8000 Aarhus C, Denmark

[§]Corresponding author. emilie.gaudry@univ-lorraine.fr

1 Introduction

Intermetallic compounds, i.e. compounds combining two or more metals or metalloids with a well-defined composition, are attracting increasing interest both for the scientific challenges they pose and for their vast potential in various applications, such as coatings and catalysts.[1] Their unique surface electronic and geometric structures can lead to enhanced catalytic performance,[2,3] as well as to reduced friction, high durability and good corrosion resistance.[4–6] The aforementioned properties are strongly influenced by adsorption. Thus, the prediction of adsorption energies on such complex surfaces is crucial to the designs of optimized compounds.

Quantitative information about adsorption is challenging to measure experimentally. First-principles methods are therefore essential to gain insights in this realm, especially to build Adsorption Energy Maps (AEMs), which establish connections between surface atomic structures and adsorption energies. AEMs offer a means to rationalize adsorbate-surface interactions and provide valuable insights into surface properties, such as adsorption energies and diffusion barriers when dealing with atomic adsorbates. AEMs are generated by computing adsorption energies at specific points of regular grids covering the considered surface.[7,8] Despite their utility, generating accurate AEMs, obtained with high-level theoretical methodologies, such as Density Functional Theory (DFT), remains challenging. This is partially due to the high computational cost of multiple geometry optimizations.[9,10] Consequently, most AEMs have been limited so far to atoms or small organic intermediates on dense metal surfaces,[11–14] although more complex systems like supported nanoparticles or nanostructured surfaces are likely to be used in practical applications.

Various methods have been developed to overcome the current limitations associated with the computational cost of adsorption energies. Methods based on chemically or physically motivated descriptors, such as the electronegativity of surface atoms,[15] the substrate density of states at the Fermi level,[16] and several d-band[17–20] or geometric features,[21,22] have proven to be quite relevant to predict adsorption energies on surfaces of elemental metals, typically by involving linear scaling.[23–26] Nonlinear approaches, such as those based on neural networks, are currently undergoing rapid and significant developments.[27] Since the first achievements – for instance the one focusing on CO adsorption on nickel[28] – many improvements have been realized,[29,30] related for instance to symmetry considerations,[31] and to global optimization protocols for surface adsorbate geometries.[32]

Data-driven methods are known to require large data sets, containing more than several hundred of DFT optimizations, such as for example $\simeq$900, $\simeq$2000, $\simeq$5000, and 42785 adsorption energies on metals or alloys in Refs.,[33–36] respectively. With the smallest data set,[33] the authors demonstrated that data-based schemes can outperform simpler models. The root mean square error (RMSE) calculated for adsorption energies on metals and binary alloys is found to be 0.15 eV, i.e. much lower than the one given by the d-band model (0.37 eV) or scaling relations (0.28 eV) on the same data set.[33] Similar results have also been obtained by simpler methods, from only three key predictors calculated with DFT (RMSE = 0.25 eV for adsorption energies of carbon species on close-packed metal surfaces),[34] or from an analytical function considering electronic factors and bonding numbers (RMSE=0.15 eV).[37] With the largest data set (Ref.[36]), the CO and atomic hydrogen adsorption energies have been calculated with an RMSE equal to 0.46 eV and 0.41 eV, respectively. More recently, state-of-the-art graph neural network models (CGCNN,[38] SchNet,[39] DimeNet++,[40,41] and MACE[42]) have been combined with huge data sets (of size 1,281,040 for OC20[43,44] and 150,000 in Ref.[42]) to build general models that can be used with any atomistic system of interest, thus popularizing the use of ML force fields. However, achieving sufficient accuracy to be useful in the field of catalysis would require a data set nearly 10 orders of magnitude larger than OC20.[44] While simple models can already give useful predictions for qualitative purposes, significant improvements of ML approaches are necessary to efficiently process large various data sets.[44]

The previous strategy, a brute-force method requiring huge data sets and aiming for applicability on a wide range of different compounds, is challenging. When dealing with AEMs, one generally focuses on a

single system, for which simple interpolations can give good results, as recently illustrated by Szilvasi *et al.*[45] Their method fully characterizes the important adsorption sites of pure platinum and pure gold nanoclusters, as well as diffusion paths, with accuracies similar to those of current approaches and at comparable computational costs. More precisely, AEMs are constructed by sampling a finite number of points forming a regular grid, and performing a spline interpolation between the calculated sites. The greater the number of points sampled, the smaller the error introduced at points where the energy has not been explicitly calculated. On binary alloy surfaces, the previous method is in line with the *surface mixing rule*, a linear interpolation of adsorption energies based on the local atomic environments around adsorption sites.[46,47] This is founded on the observation that the d-band center of the considered binary transition metal alloys is the weighted average of the d-band centers of each pure metal. Thus, using the *surface mixing rule* may be improper in the case of compounds whose structures are different from those of their pure metal constituents. This is unfortunately the case with intermetallic compounds, as illustrated by vinyl and ethylene adsorption energies at the low-index surfaces of Al_5Co_2,[48] that significantly deviate from a linear behavior.

To sum up, strategies based on machine learning can accelerate the calculation of adsorption energies. Conventional approaches, such as the d-band model, do not require huge data sets and have proven their efficiency when compared to machine learning techniques. Nevertheless, they are limited to predictions across a subset of elements with similar properties, for instance isostructural simple metals.[25] Machine learning force fields are reliable and lead to small energy prediction errors (generally below 50 meV·mol^{-1} with respect to reference ab initio values). However, they require huge training sets, even when used in combination with pretrained models, which provides a significant shortcut compared to training models from scratch.[49,50]

In the following, we focus on the (100) surface of the $Al_{13}Co_4$ quasicrystalline approximant. This compound is quite significant for potential applications as it has been identified as a cost-effective catalyst for hydrogenation,[51,52] with catalytic properties outperforming those of industrial catalysts. The surface of this compound is also attractive for its nonwetting character.[53] Finally, the related $Al_{13}Fe_4$ intermetallic is known to form at the interface of aluminum coatings on stainless steels (hot dip aluminizing of mild steel), which has major implications for coatings.[54] Three atomic adsorbates have been chosen to illustrate the performance of our approach: hydrogen, because its adsorption on catalysts' surfaces is crucial when dealing with hydrogenation reactions, oxygen, because oxide formation at catalysts' surfaces often annihilates catalytic properties and lead, because this chemical element is used as a probe to investigate the nonwetting properties of complex Al-based intermetallic substrates.[53] Through the choice of these three chemical elements, the main adsorbate-substrate bond types are considered here.

In this paper, the $Al_{13}Co_4$(100) surface is considered as a prototype of complex intermetallic surfaces with a large number of distinct adsorption sites ($n_{ads} = 46$ according to the pymatgen's AdsorbateSiteFinder tool).[11] The relevance of our approach is demonstrated through the ability to build AEMs with a number of DFT estimates smaller than n_{ads}. Computational costs are reduced by (i) carefully selecting a few relevant sites on which DFT calculations are performed and (ii) using a machine learning approach to predict adsorption energies between these sites. We show that these two ingredients outperform simple linear interpolations. Our approach offers several advantages, being both efficient and effective even with limited data, and avoiding the need to fit elaborated interaction potentials. We believe it is particularly well-suited for high-throughput exploration of adsorption sites on complex material surfaces, which paves the way for accelerating the discovery of complex functional materials such as coatings and catalysts.

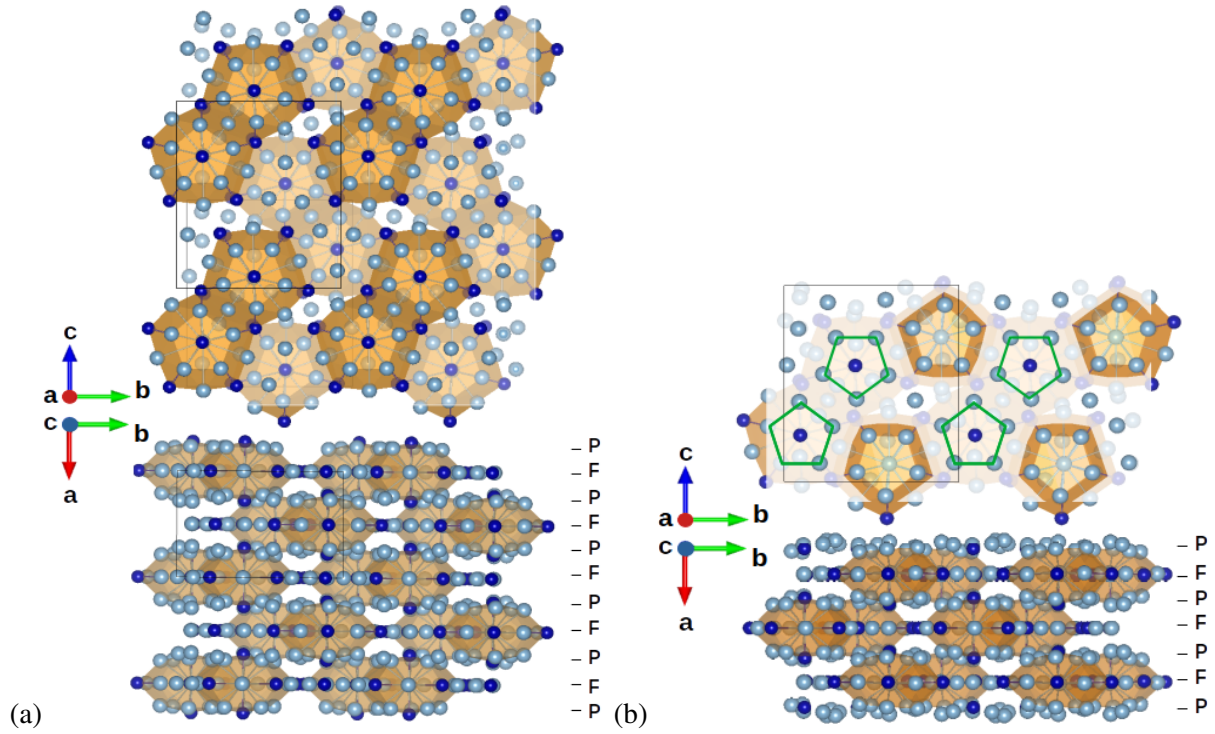

Figure 1: (a) Bulk structure of $Al_{13}Co_4$ along the [001] and [100] directions, respectively. The two types of Henley clusters are highlighted in light and dark orange. (b) Surface structure of $Al_{13}Co_4(100)$ (top and side views). Al and Co atoms are shown in light and dark blue, respectively. The crystallographic axes are shown with red, blue and green colors. The labels P and F identify puckered and flat atomic planes.

2 Details on Materials, Computations and Metrics

2.1 $Al_{13}Co_4$ Bulk and (100) Surface

The orthorhombic $Al_{13}Co_4$ phase, known as an approximant structure to decagonal d-AlNiCo quasicrystals,[55] crystallizes in the P$mn2_1$ space group (No. 31, Pearson symbol oP102). This compound is characterized by the presence of defects,[56] but here we consider the ideal structure with full atomic occupations. According to X-ray diffraction,[57,58] the bulk lattice parameters are $a = 8.158$ Å, $b = 12.342$ Å, and $c = 14.452$ Å (102 atoms per cell, Fig. 1). Atoms are arranged within two types of planes, alternating perpendicularly to the [100] direction, and usually labeled flat- and puckered planes (F- and P-type, respectively, Fig. 1a). The stacking sequence is $F_0P_{0.25}F_{0.5}P_{0.75}$ and the interlayer distance is approximately 2 Å. On the other hand, the approximant structure can be understood as a stacking of Henley-type clusters, shown in light and dark orange in Fig. 1a. The F-type planes intercept the clusters in their meridian plane.

Surface science experiments have shown that the $Al_{13}Co_4(100)$ surface consists in large terraces separated by a unique step height equal to half the lattice parameter, with no surface reconstruction either segregation. Combining the experimental observations with DFT calculations leads to the conclusion that the $Al_{13}Co_4(100)$ surface is described by P-type terminations, with vacant surface Co sites (Fig. 1b).[59–64] Bipentagonal features are resolved by scanning tunneling microscopy at the $Al_{13}Co_4(100)$ surface, and attributed to pentagonal atomic arrangements reminiscent of the ones in the bulk. They are of two types, depending on whether the centers of the bipentagons are filled with cobalt atoms (orange and green motifs in Fig. 1b).

2.2 Computational Details

DFT calculations have been performed with the Vienna ab initio simulation package (VASP).[65] Self-consistent Kohn Sham equations have been solved in the framework of the projected-augmented wave (PAW) method.[66] Spin polarization has not been taken into account, as it is not requested for such Al-rich compounds.[67,68] The electron exchange and correlation energies have been described by the generalized gradient approximation (GGA) approach, using (i) the standard semilocal functional (PBE)[69] when dealing with atomic oxygen and lead adsorbates, and (ii) the DFT-D3 method[70] in the case of atomic hydrogen adsorbates. The plane-wave energy cutoff has been set to 450 eV. Monkhorst-Pack meshes have been used for k-point sampling ($1\times7\times5$).[71] Atomic valences have been taken as $3s^2 3p^1$ (Al), $3d^8 4s^1$ (Co), $1s^1$ (H), $2s^2 2p^4$ (O), and $6s^2 6p^2$ (Pb). Total energies have been minimized until energy differences between two electronic cycles is less than 10^{-6} eV. Following our previous works,[60,72,73] the $Al_{13}Co_4(100)$ surfaces have been modeled by asymmetric 7-layer thick slabs separated by a void thickness ($\geq$ 15 Å).

Structural optimizations have been performed, and stopped when the residual Hellmann-Feynman forces on atoms were lower than 0.01 eV/Å. Two approaches have been employed to compute atomic adsorption energies (E^{nr}_{ads} and E^{r}_{ads}). On the one hand, all atoms of the slab are kept fixed to their positions in the clean slab. Only the height of the adsorbate above the surface is refined (E^{nr}_{ads}). On the other hand, both the adsorbate height and the atomic positions of the substrate top-most four layers are optimized (E^{r}_{ads}). Adsorption energies (E^{nr}_{ads} and E^{r}_{ads}) are given by:

$$E_{ads}(A,x,y) = E_{tot}(A,x,y) - E_{slab} - E_A \tag{1}$$

with $A \in \{\mathrm{H},\mathrm{O},\mathrm{Pb}\}$, $E_{tot}(A,x,y)$ the total energy of the system (slab+adsorbate) at each adsorbate's in-plane position (labeled (x,y)) and E_{slab} the energy of the clean slab. In the previous equation, E_A is defined as half of the energy of the A_2 molecule for H and O, i.e., $E_A = \frac{1}{2}E_{A_2}$, while E_{Pb} is the cohesive energy of lead. The previous adsorption energies (E^{nr}_{ads} or E^{r}_{ads}), computed on regular $\sqrt{N}\times\sqrt{N}$ grids ($N \simeq 400$) over $Al_{13}Co_4(100)$, are used to build several DFT AEMs, used as references in the following.

The deep-learning model considered for comparison purposes is MACE,[49] a high-order equivariant message-passing neural network. Training is fine-tuned from the large MACE-MP-0 model, using a specific set of hyperparameters. The same hyperparameters have been chosen here, i.e. two message-passing layers, 256 channels, with a spherical expansion of up to ℓ_{max} = 3, and 4-body messages in each layer (correlation order 3). A self-connection for both layers has been used, as well as a 128-channel dimension for tensor decomposition and a radial cutoff of 6 Å. The interatomic distances have been expanded into 8 Bessel functions multiplied by a smooth polynomial cutoff function to construct radial features, which in turn fed into a fully connected feed-forward neural network with three hidden layers of 64 hidden units and SiLU nonlinearities. A maximal message equivariance of $L = 1$ is applied. The irreducible representations of the messages have alternating parity (in e3nn notation, 128x0e + 128x1o).

2.3 Metrics

The performances of our ML model are evaluated through the root mean square error (*RMSE*), the unbiased root mean square error (*ubRMSE*), the normalized residuals (*nRES*), the Mean Absolute Error (MAE) and the Pearson correlation coefficient (*R*). Details are given in the supporting information. These metrics are defined as:

$$RMSE = \sqrt{\frac{\sum_{i=1}^{N_{test}} (\hat{E}^i_{ads} - E^i_{ads})^2}{N_{test}}}, \tag{2}$$

$$ubRMSE = \sqrt{\frac{\sum_{i=1}^{N_{test}} \left(\left(\hat{E}^i_{ads} - \langle \hat{E}_{ads} \rangle \right) - \left(E^i_{ads} - \langle E_{ads} \rangle \right) \right)^2}{N_{test}}}, \tag{3}$$

$$nRES(\hat{E}^i_{ads}) = \frac{|\hat{E}^i_{ads} - E^i_{ads}|}{\sigma(\hat{E}_{ads})} \tag{4}$$

$$MAE = \frac{\sum_{i=1}^{N_{test}} |\hat{E}^i_{ads} - E^i_{ads}|}{N_{test}} \tag{5}$$

$$R = \frac{\sum_{i=1}^{N_{test}} (E^i_{ads} - \langle E_{ads} \rangle)(\hat{E}^i_{ads} - \langle \hat{E}_{ads} \rangle)}{\sqrt{\sum_{i=1}^{N_{test}} (E^i_{ads} - \langle E_{ads} \rangle)^2} \sqrt{\sum_{i=1}^{N_{test}} (\hat{E}^i_{ads} - \langle \hat{E}_{ads} \rangle)^2}} \tag{6}$$

In the previous equations, $\hat{E}^i_{ads}$ and E^i_{ads} are the predicted and DFT adsorption energies on sites i of the test set, whose cardinal is N_{test}. The corresponding averaged values of $\hat{E}^i_{ads}$ and E^i_{ads} are $\langle \hat{E}_{ads} \rangle$ and $\langle E_{ads} \rangle$, respectively. Energies can be relaxed or nonrelaxed quantities (E^{nr}_{ads} or E^r_{ads}) depending on whether the DFT calculations are performed by fixing or relaxing surface atoms, as mentioned in Sec. 2.2. The standard deviation σ is computed for predicted values ($\hat{E}^i_{ads}$). Note that the lower *RMSE*, *ubRMSE*, *MAE* or *nRES*, and the larger R, the better the accuracy.

Finally, box-and-whisker plots are used to display the distribution and variability of our predictions. The box represents the interquartile range of the data set, which contains the middle 50% of the data. A plain line at the median divides the data set into two equal halves. The whiskers extend from the box to show the range of the data, excluding the outlier data points. Beyond the whiskers, the data are considered as outliers and are plotted as individual points.

3 Method

Fig. 2 summarizes our machine learning (ML) workflow to predict adsorption energies. Additional details are given in the supporting information. We first define a set of pairs made of a smooth overlap of atomic positions (SOAP)[74,75] descriptor centered at the position of the adsorbate and the associated adsorption energy (E^{nr}_{ads} or E^r_{ads}). Parameters related to the descriptors are detailed in the supporting information (section S1). To limit the number of costly DFT steps required to obtain both the adsorbate energies and their optimized z-coordinate at each (x,y) position, only a few (x,y) sites, carefully selected (Sec. 3.1), are considered for the DFT optimizations. Moreover, all data produced during the DFT relaxation process are included in the training set (Sec. 3.2), i.e. between 5 and 40 energies for each (x,y) position, depending, among others, on the number of atoms allowed to relax. Our predictions are assessed by computing metrics on test sets made of the adsorbate's optimized positions and the associated DFT energies (E^r_{ads} or E^{nr}_{ads}, Sec. 3.2).

3.1 Site Selection

Our ML approach aims to drastically decrease the computation costs, by learning the adsorption energies of a few number of sites. To ensure good generalization performances from a limited data set, sites selected for the training step should provide a large variety of different configurations. Sampling based on standard molecular dynamic trajectories leads to impractically long computational times attributed to the presence of large free energy barriers.[76] Random sampling is not an option here, as it is not possible to guide the selection process in such a high-dimensional feature space. Therefore, it is necessary to design efficient algorithms that are able to accelerate phase space exploration. It is worth to mention that this selection should be made on nonrelaxed (initial) systems, prior to any DFT computation, to reduce computational costs.

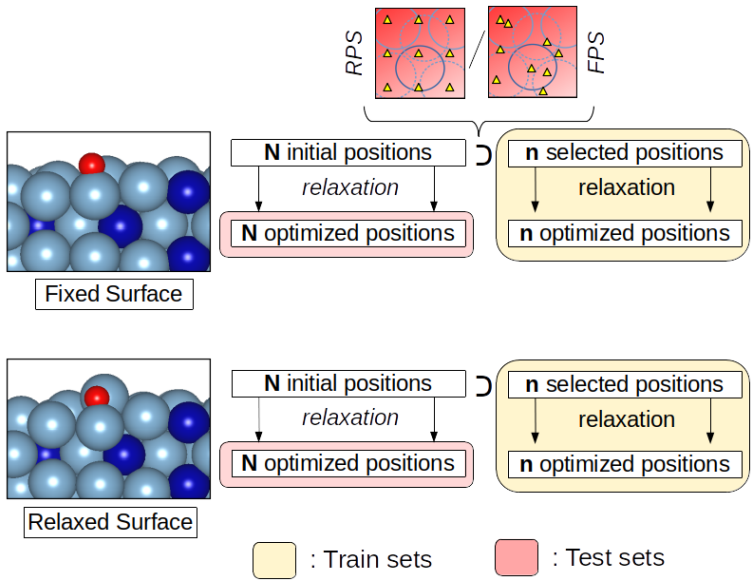

Machine learning workflow (a)

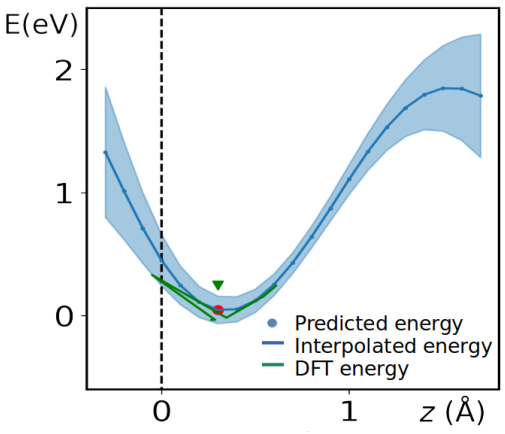

Typical shape of E_{ads}^{nr} for atomic hydrogen as a function oh the height's adsorbate (b)

Figure 2: (a) Machine learning workflow. From N positions distributed on a regular $\sqrt{N} \times \sqrt{N}$ grid over the surface, n positions are selected, either on a regular subgrid, or through the so-called Farthest Point Sampling (Sec. 3.1). DFT calculations are achieved to get adsorption energies , through the optimization of the adsorbate height (z-coordinate) for a given (x,y) position. The training set is made of all pairs of descriptors centered at the nonrelaxed adsorbate position together with adsorption energies (Sec. 3.2). The test set is made of the DFT optimized positions from all of the N initial positions together with the associated adsorption energies. Two possibilities are explored: the surface is either relaxed or not (Sec. 3.2). Color code of structural models : Al (light blue), Co (dark blue), and O (red). (b) Adsorption energies, as a function of the adsorbate height, plotted here for atomic hydrogen located at one favorable site, i.e., $(x,y) = (3.68$ Å, 12.14 Å). Predicted ($\hat{E}_{ads}^{nr}$) and DFT (E_{ads}^{nr}) values are shown in blue and green, respectively. Spline interpolation between predicted values is plotted in blue (straight line). The standard deviation of the GPR is also shown (blue area). The dashed vertical black line represents the position of the underlying atoms in the termination plane. The red dot indicates the height selected by our algorithm.

We propose to make the selection from a set of N regularly spaced sites (x_i, y_i) $(1 \leq i \leq N)$, located in a two-dimensional plane defined by its z-position (z_0) in the simulation box. We choose a regular sampling of $\sqrt{N} \times \sqrt{N}$ sites, with $\sqrt{N} = 20$ ($N = 400$) in the case of atomic hydrogen and oxygen, and with $\sqrt{N} = 19$ ($N = 361$) for atomic lead. Let us note that D_i is the SOAP descriptor at the position (x_i, y_i, z_0), where $z_0 = 1$ Å for atomic hydrogen and $z_0 = 2$ Å for atomic oxygen and lead, the reference being defined by the position of the termination plane. The Euclidean distance d_{ij} measures the dissimilarity between the descriptors at positions (x_i, y_i, z_0) and (x_j, y_j, z_0). Let us note $\mathbb{D}_m$ the set of the indices of the m first selected sites among the above-mentioned $\sqrt{N} \times \sqrt{N}$ sites. The set $\mathbb{D}_m$ is built recursively:

- The first selected site minimizes the average distance between the descriptor computed from this site and all other descriptors, thus: $\mathbb{D}_0 = \{i_0\}$, with

$$i_0 = \underset{i \in \{1,\ldots,N\}}{\operatorname{argmin}} \sum_{1 \leq j \leq N} d_{ij} \tag{7}$$

  In other words, the descriptor D_{i_0} is the medoid of the set of all descriptors computed from the sites of the regular grid.

- For any $m \geq 0$, the $m+1$-th selected site has the descriptor with the largest dissimilarity to the descriptors of the sites already selected in $\mathbb{D}_m$. We measure the dissimilarity between the descriptor D_i and the descriptors from $\mathbb{D}_m$ as $\min_{j \in \mathbb{D}_m} d_{ij}$. That is, $\mathbb{D}_{m+1} = \mathbb{D}_m \cup \{i_{m+1}\}$, with

$$i_{m+1} = \underset{i \in \{1,\ldots,N\} \setminus \mathbb{D}_m}{\operatorname{argmax}} \min_{j \in \mathbb{D}_m} d_{ij} \tag{8}$$

  where $A \setminus B$ denotes the set of elements that are in a set A but not in a set B.

  In other words, we add an $m+1$-th site that is likely to introduce new pieces of information as its atomistic environment is dissimilar to the ones from the sites in $\mathbb{D}_m$.

Our selection strategy is similar to the Farthest Points Sampling (FPS) method widely used in literature.[32,77,78] For comparison purposes, we choose n as a square number (n = 9, 16, 25, 36, 49, 64, 81, 100), since ML models will be trained using data sampled either using the FPS method or from a Regular two-dimensional $\sqrt{n} \times \sqrt{n}$ Point Sampling (RPS) of the surface cell. To avoid any dependence of the test metrics on the position of the substrate relative to that of the grid, we considered standard deviations resulting from systematic in-plane translations of the grid, leading to confidence intervals rather than a unique value when calculating the metrics defined in Sec. 2.3.

The distribution of sites selected by the FPS method is shown in Fig. 3 for $n = 49$ (yellow triangles displayed in the right-hand panels). Selected points, distinct for the three considered systems due to tiny differences between grids, are nonequivalent from a crystallographic point of view. They do not span the surface cell in a uniform way, and do not systematically mirror the most stable adsorption sites. By comparing the sites selected for various n values – those for $n \in \{9, 25, 49\}$ are shown in Fig. 4, and all data are gathered in the supporting information, section S2 – one can also notice that singular sites are systematically selected at the beginning of the selection process, such as the position on top of the protruding Co atom, the center of the Al bipentagonal motifs or the center of the 4-fold sites between to bipentagons.

3.2 Training and Prediction

DFT computations are performed for adsorbates located at the n relevant sites identified previously by the FPS and RPS methods. As already mentioned, all data produced during the DFT relaxation process are included in the training set. Training is performed through the Gaussian Process Regression (GPR)[79,80] and a Gaussian kernel. Parameters are detailed in the supporting information (section S1). The probabilistic nature of the GPR automatically leads to confidence intervals for predicted values, while other regression methods, such as the kernel ridge or the support vector regression, require time-consuming additional bootstrap approximations to estimate confidence bounds.

Once training is completed, adsorption energies are predicted at each site i of a regular two-dimensional $2\sqrt{N} \times 2\sqrt{N}$ grid spanning the $Al_{13}Co_4(100)$ surface for several different heights in the range $[z_{min}(x_i, y_i)$; $z_{max}(x_i, y_i)]$. We take $z_{min}(x_i, y_i) = d_S(x_i, y_i) - a$ where a =0.30 Å and $d_S(x_i, y_i)$ is the sum of the covalent radii of species involved at the considered site (in Å). We choose $z_{max}(x_i, y_i) = z_{max}$ =2.23 Å. Typically, for each site i, the predicted adsorption energy varies as shown in Fig. 2b, i.e. it shows a minimum value. The z-coordinate $z_{opt}(x_i, y_i)$ that minimizes the predicted energies is identified (red dot in Fig. 2), and the corresponding adsorption energy is calculated. It can happen that no minimum can be found. In that case, $z_{opt}(x_i, y_i)$ is set to the value corresponding to the lowest predicted energy, i.e. $[d_S(x_i, y_i) - a]$ or z_{max}. Finally, the performance of our machine learning setup is quantified through the metrics defined in Sec. 2.3, using the equation $N_{test} = N$.

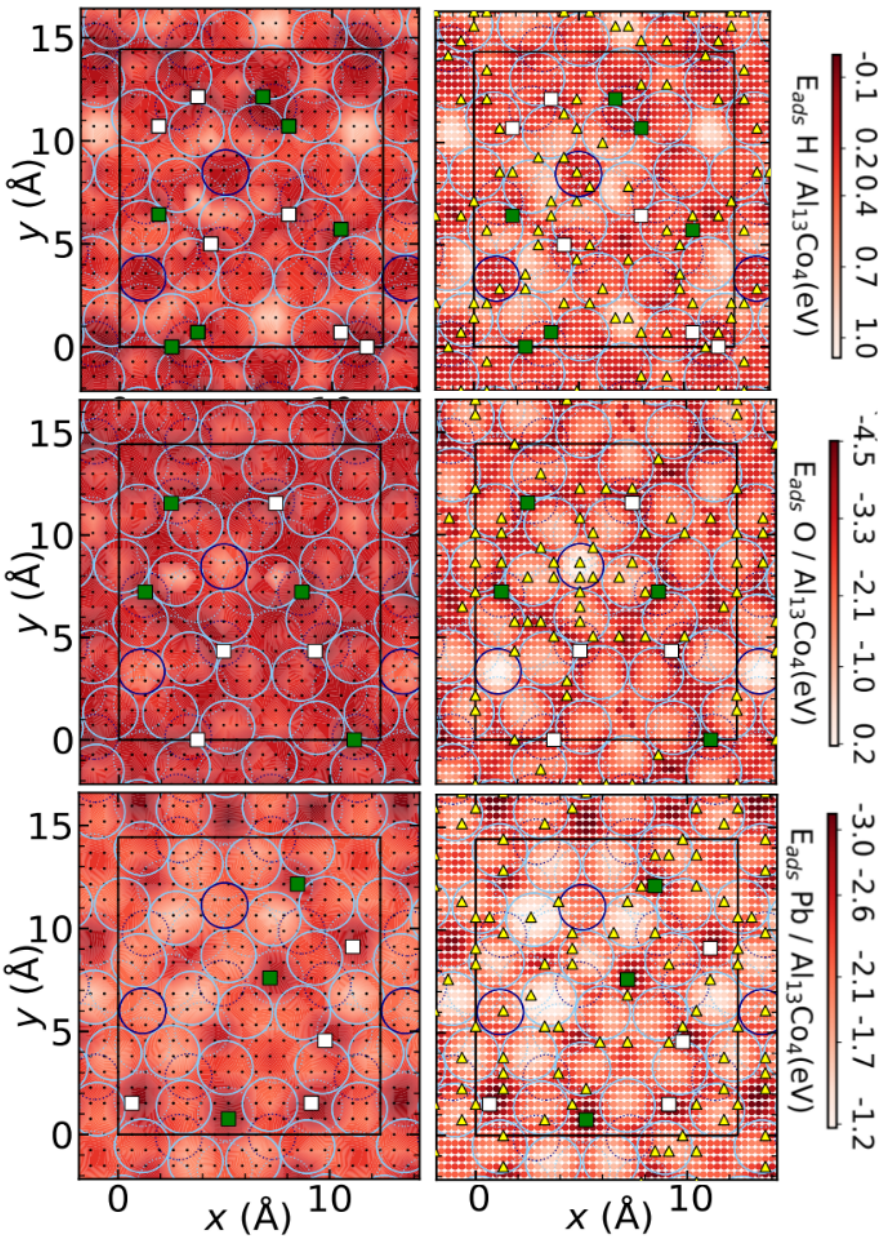

Figure 3: DFT (E^r_{ads}) and predicted ($\hat{E}^r_{ads}$) AEMs for H (first row), O (second row) and Pb (third row) adsorbates when $n = 49$. Green and white squares indicate the most favorable adsorption sites according to DFT. Small black dots show the sites on which DFT calculations have been performed. The surface atomic structures are superimposed on the AEMs. Light and dark blue circles represent Al and Co atoms, respectively, at the termination plane (solid lines) or at the subsurface plane (dotted lines).

4 Results and Discussions

Adsorption energy maps are conventionally plotted by interpolations between dense point grids. Based on the $\sqrt{N} \times \sqrt{N}$ regular grids mentioned before (Sec. 3.1), two DFT maps for each adsorbate (E^{nr}_{ads} and E^r_{ads}) have been plotted (Figs. 3, S3, S14, S25). The most favorable adsorption sites for each element have been highlighted with green and white squares. They are gathered by pairs, due to the presence of a 2-fold

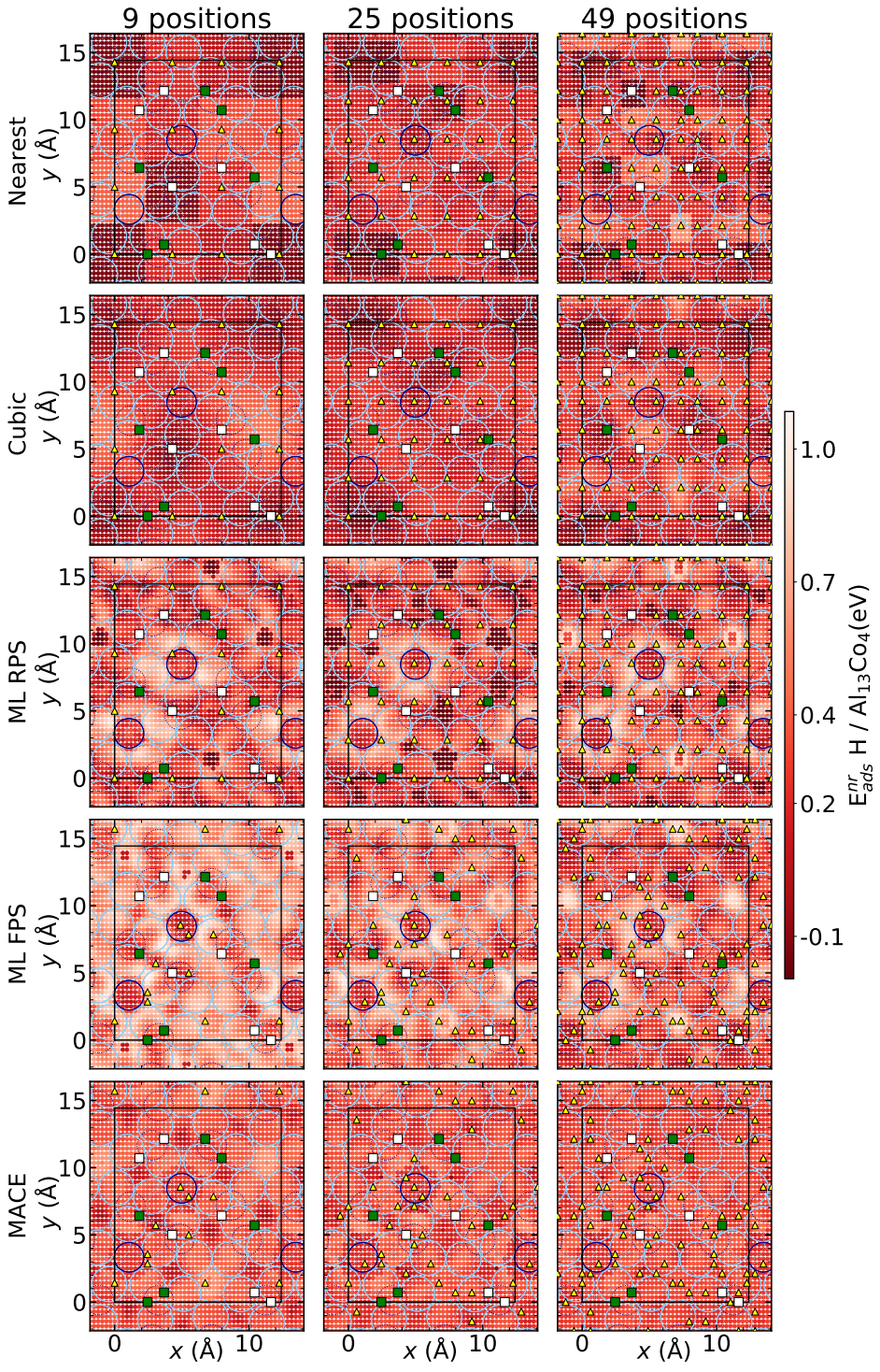

Figure 4: Adsorption energy maps (E^r_{ads}) for atomic hydrogen. Predictions based on different methods (interpolations, RPS and FPS ML, MACE ML) and different sizes of the training sets (n = 9, 25, 49) are considered. Yellow triangles indicate the sites on which DFT calculations are performed. Green and white squares show the most stable sites for H adsorption, according to DFT. The surface atomic structures are superimposed on the AEMs. Light and dark blue circles represent Al and Co atoms, respectively, at the surface (full lines) or the subsurface (dotted lines).

axis perpendicular to the surface plane whose trace is located in the center of the 4-fold site between two pentagonal motifs. Favorable sites for atomic hydrogen are found among bridge Al-Al sites, stabilized by a subsurface Co atom, in agreement with a previous work.[81] Atomic oxygen adsorbs preferentially at 3-fold hollow sites of $Al_{13}Co_4$(100), which is consistent with the O chemisorption sites on Al(111) in the 3-fold coordinated fcc positions.[82] Favorable sites for atomic lead are found in large hollow sites, in agreement with previous works.[73,83]

4.1 Exploring Adsorption Energy Maps

Whatever the data selection used for training, the general appearance of the DFT AEMs (Figs. 3,4, S4, S15, and S26) is nicely reproduced by our ML approaches. In particular, 5-fold symmetries around the protruding Co atoms, are well rendered, even with a very small number of training data ($n = 9$). In contrast, interpolation methods, based either on nearest neighbor approaches, which estimate the adsorption energies by assigning to a position the value of the nearest known point in the AEM, or on cubic interpolations, which involve third-order polynoms, fail to correctly reproduce the 5-fold symmetry around the protruding Co top-most atoms, even with $n = 49$. In addition, we can notice that equivalent sites, connected through the 2-fold symmetry mentioned above, can be interpolated with different values when n is small, while this pitfall is avoided with ML methods. We also discuss our approach in relation to the MACE force field built by fine-tuning MACE-MP-0, i.e. by using the primary parameters of MACE-MP models and by retraining them with the new structures. The MACE energy landscape appears to be much flatter than the one calculated by DFT. This is attributed to the small size of the training set used for the fine tuning, which is probably too small to manage the huge number of degrees of freedom related to the relaxation of both the adsorbate and surface atoms. As a consequence, the 5-fold symmetry features are much less visible using the MACE ML than with FPS and RPS MLs.

A detailed analysis shows that energies are better predicted when a similar environment is included in the training set. For instance, adsorption at surface Co vacancy sites is correctly predicted by FPS even when $n = 9$, since one of these sites – $(x,y) = (7.44$ Å, 1.44 Å) – is among the first position selected, i.e. it is included in the training set when $n = 9$. Thus, for hydrogen, the relevance of our ML approach can be understood by the fact that the first sites selected for training (FPS method) are top Co, top Al, bridge Al-Al, bridge Co-Al, hollow Al sites, i.e. the typical adsorption sites on metal surfaces. In contrast, training based on regular grids fails to give the correct value when $n = 9$ because no learning is done at this site when $n < 49$. For oxygen, the noncorrect predictions by RPS ML on top Co atoms when n is small can be explained by not including top Co sites in the training set when $n = 9$ and $n = 16$. A similar explanation is valid for vacancy sites in the case of lead.

The qualitative comparison between DFT-based and ML-predicted AEMs shows that FPS and RPS ML outperform interpolation strategies, especially when $n \leq 36$. These observations are clearly measured by the R-factor (Figs. 5).Overall, for all adsorbates, the R-factor increases with n, and is higher when predictions are made using our ML method than simple interpolations (Figs. S12, S23, and S34). For $n = 9$, the Pearson-R is $\simeq 0.4$ (ML) versus $\simeq 0.1$ (interpolation), $\simeq 0.6$ (ML) versus $\simeq 0.1$ (interpolation) and $\simeq 0.6$ (ML) versus $\simeq 0.2$ (interpolation) for H, O and Pb, respectively. The consideration of other metrics are also in favor of the ML approach (Figs. S12, S23, and S34), especially when $n \leq 36$, which is the range of interest when aiming to identify favorable adsorption sites with a number of DFT calculations lower than that suggested by the pymatgen triangulation method (n_{ads} = 46).[11] These other metrics are discussed below (Sec. 4.2) .

4.2 Benchmark of Metrics

Within our ML scheme, only the z-position of the atomic adsorbate is optimized, with all surface atoms being frozen at their positions in the clean surface. However, surface relaxations, occurring upon adsorption,

stabilize the whole system and thus strengthen energies (Figs. S13, S24, S35). Overall, the difference between E_{ads}^{nr} and E_{ads}^{r} results in an energy shift, equal to 180, 900, and 200 meV, on average, for H, O, and Pb, respectively, with variations depending on the adsorption site and the adsorbate. Differences between E_{ads}^{nr} and E_{ads}^{r} are the largest in the vicinity of protruding Co atoms for H, while they are on top of one surface Al atom between protruding Co for Pb. For oxygen, the surface relaxation exhibits a much greater intensity and cannot be described by a simple energy shift. It affects most sites, especially Al top sites belonging to the pentagonal motifs centered with Co (in orange in Fig. 1). Thus, in this work, training is performed on either relaxed or nonrelaxed energies, while metrics are calculated with reference to relaxed or nonrelaxed DFT values. In all cases, systematic comparisons are summarized in the supporting information (Figs. S4-S12 for H, Figs. S15-S23 for O, Figs. S25-S34 for Pb).

Metrics measured on nonrelaxed systems show clearly that ML outperforms interpolation strategies, especially for small n values. When $n = 49$, the RMSE related to the prediction of H adsorption (E_{ads}^{nr}) is 0.07 eV, 0.15 eV, and 0.16 eV for ML, cubic and nearest interpolation methods, respectively, Figs S8, S12, S20, S23, S31, and S34). The RMSE decreases quickly with n, especially between $n = 9$ and $n = 36$. The metrics are degraded when moving from E_{ads}^{nr} to E_{ads}^{r} (Figs. 5, S8, S20, and S31). For hydrogen, this is clearly illustrated by the ubRMSE, which is larger than 0.1 for any $n \leq 100$. Similar trends are also observed for lead (Fig. 5a). More precisely, the ubRMSE measured for FPS-ML, interpolation-based and MACE-ML predictions are 0.15, 0.17, and 0.17 eV, respectively, for hydrogen and 0.17, 0.25, and 0.22 eV for lead when $n = 36$. In the case of oxygen, all methods lead to values roughly equal to 0.5 eV (0.55, 0.47, and 0.46 eV, respectively) due to large surface relaxations in this case. Despite the high RMSE values, we observe a good correlation between predicted (FPS-ML) and ground-truth DFT values in terms of the Pearson coefficient (0.73, Fig. 5b). Finally, histograms of normalized residuals, plotted for the atomic H, O and Pb adsorbates (Fig. 5c), show a Gaussian shape for the three elements. This suggests that no specific statistical feature influences the results, especially for oxygen.

The worse metrics are obtained for the predictions of oxygen adsorption. It is not so surprising, as similar observations have already been reported.[84] On transition metal surfaces, the MAE for O adsorption has been calculated to be 0.16 eV,[84] i.e. it is twice the MAE for H adsorption (0.08 eV). On bimetallic alloy surfaces, according to Ref.,[9] the MAE for H adsorption is measured to be 0.07 eV, while it is 0.15 eV for O adsorption. A possible explanation for such a behavior may be the specific bond between the surface and oxygen, involving strong charge transfers and surface relaxations. Our model is based on a local geometric descriptor, that neither considers surface relaxation nor takes global changes in the electronic structure into account. Methods developed recently, such as those using a fourth-generation high-dimensional neural network potential that combines a charge equilibration scheme employing environment-dependent atomic electronegativities with accurate atomic energies, may help to go beyond the current limitations.[85]

The metrics measured in this work are of the same order of magnitude as those provided by other approaches. For atomic hydrogen the literature has reported MAEs ranging from 0.07 eV[9] to 0.24 eV[36] with many studies falling in between those values.[35,77,84,86–90] In the present study, similar values have been obtained, but with a data set that is (much) smaller. For instance, the RMSE for atomic hydrogen adsorption is measured to be 0.075 eV, based on a training data set containing around 10000 DFT single-point calculations, spanning adsorption sites on the surface of 91 MoS_2 clusters.[77] A RMSE decreasing from 0.1 eV, down to 0.052 eV when focusing on a specific set of sites, are obtained using various ML algorithms trained over approximately 5000 configurations of Ag alloys,[35] and over 6477 configurations of nitrogen-doped carbon nanotubes.[89] This is slightly larger than the value of 0.03 eV obtained with 100 positions in our training set (RMSE, E_{ads}^{nr}, $n = 100$) and of the same order of magnitude than the value obtained with $n = 64$ (RMSE, E_{ads}^{nr}). The relevance of the FPS combined with SOAP descriptors is shown to be relevant to treat small data sets, as shown by the results based on 1400 DFT single-point calculations to predict hydrogen adsorption on metallic nanoclusters.[90] In their work, the MAE of the predictions is around 0.1 eV, i.e. comparable to that obtained with $n = 25$ in this work.

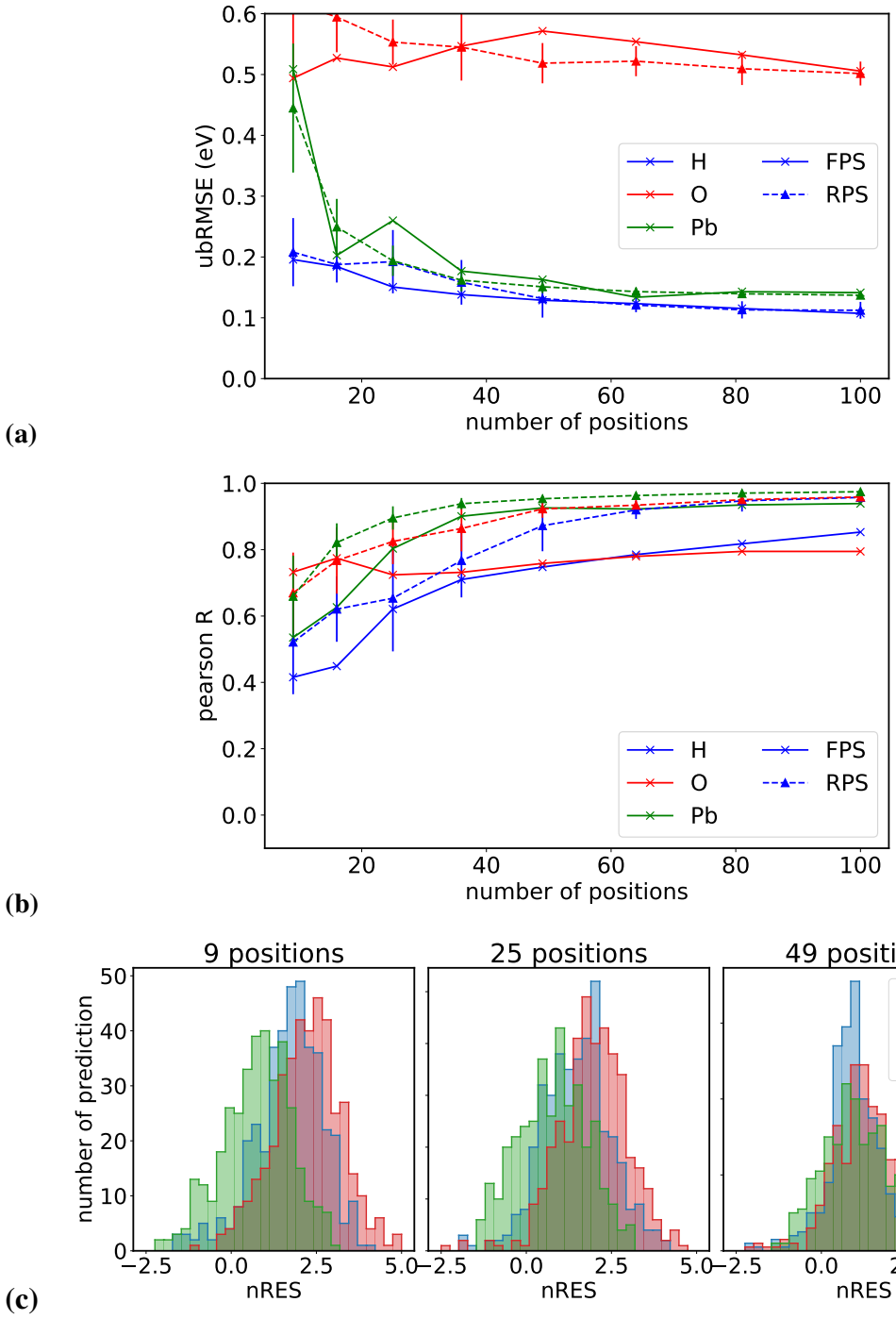

Figure 5: (a,b) Metrics related to the prediction of adsorption energies (E^r_{ads}). The RMSE (a) and Pearson coefficient (b) are plotted as functions of n for both RPS (dashed line) and FPS (solid line). (c) Histograms of errors by FPS. Color code : H (blue), O (red) and Pb (green).

4.3 Farthest versus Regular Point Samplings

Roughly, the FPS and RPS ML methods give similar qualitative results. Nevertheless, we can notice few differences between the two ML AEMs, especially when n is small. For instance, noncorrect predictions,

identified by dark red regions in Figs. S4, S15 and S26, more frequently occur with RPS than FPS. This is better illustrated by $\Lambda(n)$ (Fig. 6), the number of predictions with a stronger binding energy than those corresponding to the most stable site identified by DFT, within a spatial resolution of 1.04 Å × 1.44 Å. Indeed, since our approach aims to predict the most stable adsorption sites on a complex surface, a high-performance and relevant algorithm would predict correctly the sites with the stronger adsorption energy. Thus, the $\Lambda(n)$ number evaluates the reliability of the prediction of most stable adsorption sites. For hydrogen, $\Lambda_{\mathrm{H}}^{FPS}(n)$ is null for $n > 16$, while $\Lambda_{\mathrm{H}}^{RPS}(n) < 1$ only when $n \geq 64$. For oxygen, noncorrect predictions using RPS ML occur on the top Co atoms when $n = 9$ and $n = 16$ (Fig. S15). FPS leads to more reliable predictions than RPS, with $\Lambda_{\mathrm{O}}^{FPS}(9) = 10$ and $\Lambda_{\mathrm{O}}^{FPS}(i) = 0$ for $i \geq 16$, while $\Lambda_{\mathrm{O}}^{RPS}(i) \leq 1$ for $i \geq 36$. For lead, noncorrect predictions using RPS ML occur at surface vacancies when $n = 9$ and $n = 16$ (Fig. S26). Here, FPS also shows noncorrect predictions, especially in the vicinity of protruding Co atoms, but without impacting the identification of most stable sites, since $\Lambda_{\mathrm{Pb}}^{FPS}(n) = 0$ for any n. In contrast, $\Lambda_{\mathrm{Pb}}^{RPS}(i) > 1$ for $i < 25$.

We also compared the regular and farthest point samplings using other metrics. Fig. 6 shows normalized residuals for H/$Al_{13}Co_4$(100) (E_{ads}^{nr}, n = 9, 25, 49). Additional results are gathered in the supporting information, in Figs. S5-S8 for H, S16-S19 for O and S27-S30 for Pb. Focusing on atomic hydrogen (E_{ads}^{nr}), the largest errors by FPS are found in the regions of low Co content. This can be attributed to the fact that, when n is small, FPS overrepresents environments with Co top-most atoms in the training set. Thus, it induces a systematic bias, slightly overestimating adsorption energies for most positions, that is mostly overcome when $n = 49$ by including more Al environments. In contrast, errors are more homogeneously distributed when using RPS. However, in that case, histograms show that the adsorption energies of a small number of sites are predicted with large errors. Fig. 6 shows large (negative) pitfalls, that lead to a considerable underestimation of adsorption energies for small n values. These outliers arise during the energy minimization, by a failure in finding the optimal adsorbate's height ($z_{opt}(x_i, y_i)$). Quantitatively, the deviation computed by FPS (0.190 eV when n =9) is a bit larger than the one obtained by RPS (0.174 eV). The RPS interquartile range is also smaller than the FPS one, both decreasing when n increases: 0.313 and 0.172 eV with $n = 9$; 0.027 and 0.029 eV with $n = 100$. This can be understood by the fact that for small n values, the RPS selection method is almost as efficient as a random selection. Most common sites, i.e. Al rich sites, are chosen for training, in this case, and singular sites are discarded. Conversely, first sites selected through FPS are unique sites, aiming to account for the large diversity of surface adsorption sites. As a consequence, overall, for very small n values, AEMs are barely better predicted by RPS (Fig. 6a), and they lead to a bit more regular histograms (Fig. 6b) and narrower interquartile ranges (Fig. 6c)). However incorrectly favorable sites are identified. The situation is clearly inverted in the range $25 \leq n \leq 64$, because the FPS training set is large enough to more comprehensively address the AEM complexity while the RPS selects more equivalent sites. For $n \geq 81$, the results are similar for both RPS and FPS methods. In summary, while metrics are slightly better for RPS than for FPS for very small n values, large (negative) pitfalls arise by RPS, which results in a sizable underestimation of adsorption energies, which makes it prohibitive to identify the most favorable adsorption sites.

5 Conclusions

In this work, machine learning was performed to explore adsorption energy landscapes of $Al_{13}Co_4$(100). The proposed approach efficiently identifies most favorable adsorption sites, with a few DFT estimates. The Farthest Point Sampling method, which selects sites on which DFT calculations are performed, avoids redundancy in small training sets, as well as large errors on predictions. In contrast to RPS, it does not depend on the relative position of the sampling grid with respect to the surface, and thus avoids the variability observed in RPS-based predictions, this phenomenon being critical with small data sets (typically $n \leq 49$). Most favorable adsorption sites are correctly identified, and energies are predicted with an acceptable RMSE for H, O,

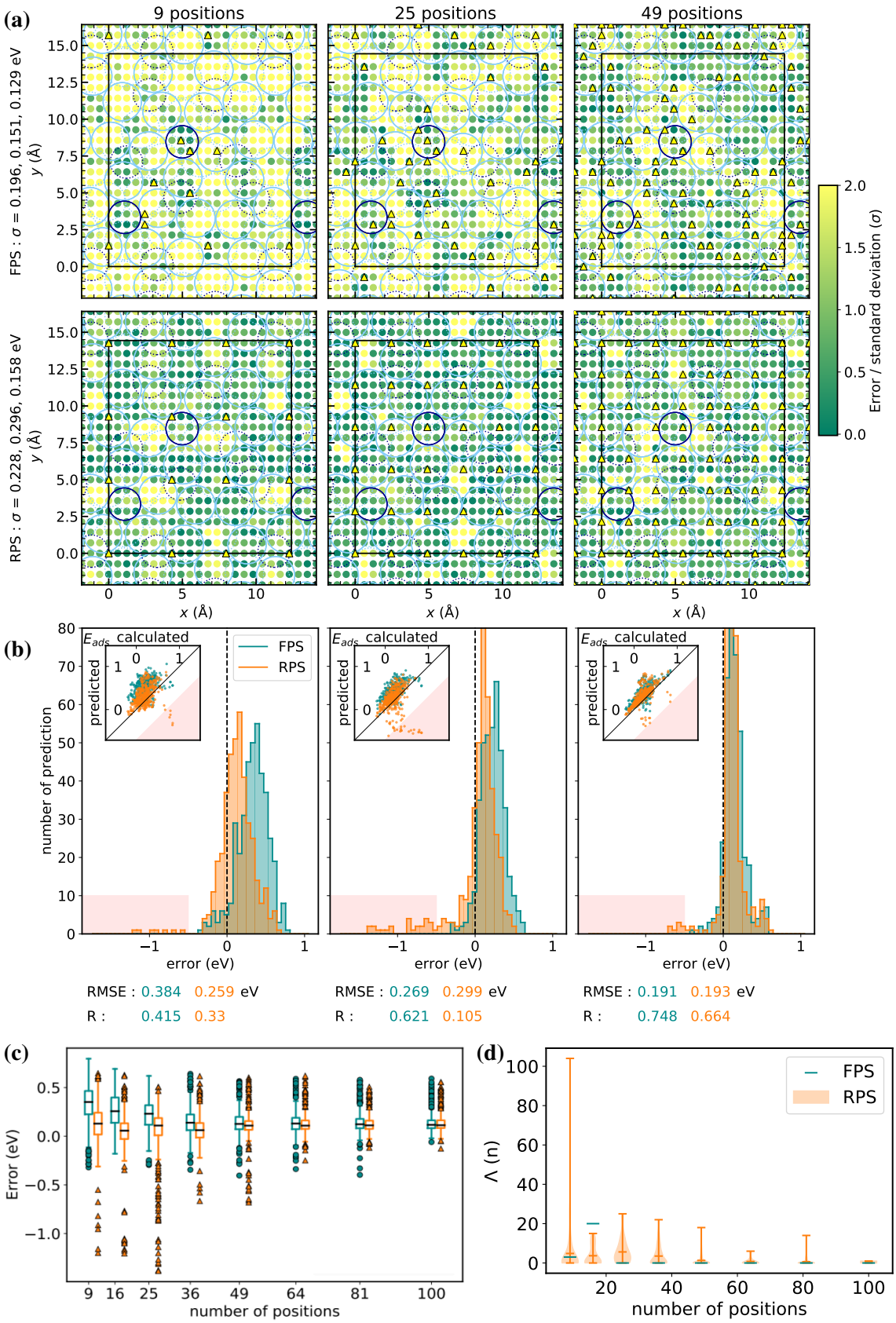

Figure 6: Comparison of the sampling methods – FPS (cyan) vs RPS (orange) – on predictions of H adsorption energies. Training is performed using relaxed adsorption energies (E^r_{ads}), calculated by DFT on sites highlighted by yellow triangles. Results are compared to E^r_{ads}. (a) Residual error maps. Light blue circles represent Al atoms at the surface (full lines) or subsurface (dotted lines). (b) Errors histograms and corresponding parity plots. Errors larger than 0.5 eV are highlighted by the red area. (c) Whisker plots of errors for all n. (d) $\Lambda(n)$ (see the text for details) measured for FPS (cyan) and RPS (orange). The violin plot shows the data distribution related to the relative position of the grid to the surface.

and Pb adsorbates : 0.27, 1.16, and 0.25 eV for E^r_{ads} and 0.14, 0.37 and 0.15 eV for E^{nr}_{ads}, respectively, with $n = 16$. Enriching the training set greatly improves the metrics, since the RMSE decreases to 0.03 and 0.02 eV for H and Pb adsorption (E^{nr}_{ads}) when $n = 100$. The computational cost to train the proposed ML algorithm is very low, of the order of one hour for $n = 100$. This is negligible compared to the computational cost of DFT (between 150 000 and 600 000 CPU hours for the AEM built from DFT calculations performed on 400 sites for hydrogen, using E^{nr}_{ads} and E^r_{ads}, respectively). The chemistry and physics of the system are shown to influence the performance of our model. Indeed, the strong Al-O bond induces large surface relaxations, which are highly dependent on the adsorption site, and that are difficult to capture with a model relying on local geometric features and that only optimizes the adsorbate's height with respect to the surface.

The proposed ML method outperforms not only simple interpolation schemes for small n values, but also one force field neural network (MACE). It does not aim to train a universal model from a huge database, but focuses on specific systems, like the one developed in this paper, where the effort required to adapt a machine learning potential would be too great. This targeted approach ensures accurate and reliable results, even with minimal data, making it highly effective for specific complex systems.

Our approach offers notable advantages, being both efficient and effective even with limited data, making it particularly well-suited for high-throughput exploration of adsorption sites on complex material surfaces. Further developments will aim to better entangle relaxations, possibly with the consideration of electronic features. The transferability of our model should also be investigated, by simultaneously predicting adsorption on multiple surface orientations.

6 Acknowledgments

This work was granted access to the High Performance Computing (HPC) resources of IDRIS and TGCC under the allocation 99642 attributed by GENCI. HPC resources were also partially provided by the EXPLOR center hosted by the University de Lorraine (project 2017M4XXX0108). The authors thank Dr. Thiago Dorini and Corentin Chatelier for their initial contribution related to AEMs. This work is supported by the European Integrated Center for the Development of New Metallic Alloys and Compounds. We acknowledge financial support from the European Union under the program FEDER-FSE Lorraine et Massif des Vosges 2014-2020 (COMETE project, COnception in silico de Matériaux pour l'EnvironnemenT et l'Énergie), from "Lorraine Université d'Excellence" and from ANR (project LOR-AI ANR-20-THIA-0010).

7 Associated Content

Data Availability Statement and Code Availability DFT data and software codes are available at the following URL:
`https://gitlab.univ-lorraine.fr/gaudry6/machinelearning_ijl.git`

We added a working example that calculates the AEM for atomic hydrogen on Ag(111). Density functional calculations have been performed on only three sites, identified by FPS (yellow triangles), and lead to 19 single point calculations. All atoms in the three-layer thick slab are kept fixed to their bulk positions. Our results for the top, fcc, hcp, and TS sites are consistent with those of Ref.[91] Results are provided as well, through the adsorption energy map, as well as through the energy profile of the diffusion path atop $\rightarrow$ fcc $\rightarrow$ bridge $\rightarrow$ hcp $\rightarrow$ atop. The latter diffusion profile is found in good agreement with the literature, errors on the four barriers mentioned above being less than 12% and 8% (with a training set containing DFT relaxations performed using 3 and 7 surface sites, respectively).[91]

Supporting Information The Supporting Information is available free of charge at `https://pubs.acs.org/doi/XX`

S1 Machine learning details : SOAP descriptor, Gaussian Kernel, Metrics, MACE setup. S2 Results : Adsorption energy maps, Error maps and histograms, Metrics, including $\Lambda(n)$ for H, O and Pb on $Al_{13}Co_4$.

References

[1] D. C. Fredrickson and G. J. Miller. Intermetallic chemistry: New advances in humanity's age-old exploration of metals and alloys. *Acc. Chem. Res.*, 51:213, 2018.

[2] S. Furukawa and T. Komatsu. Intermetallic Compounds: Promising Inorganic Materials for WellStructured and Electronically Modified Reaction Environments for Efficient Catalysis. *ACS Catal.*, 7:735–765, 2017.

[3] M. Armbruester. Intermetallic compounds in catalysis - a versatile class of materials meets interesting challenges. *Sci Technol Adv Mater.*, 21:303, 2020.

[4] J. Ledieu, M. Krajčí, J. Hafner, L. Leung, L. H. Wearing, R. McGrath, T. A. Lograsso, D. Wu, and V. Fournée. Nucleation of Pb starfish clusters on the five-fold Al-Pd-Mn quasicrystal surface. *Physical Review B*, 79:165430, 2009.

[5] B. Unal, J. W. Evans, T. A. Lograsso, A. R. Ross, C. J. Jenks, and P. A. Thiel. Terrace-dependent nucleation of small Ag clusters on a five-fold icosahedral quasicrystal surface. *Philosophical Magazine*, 87:2995–3001, 2007.

[6] S. C. Deevi. Advanced intermetallic iron aluminide coatings for high temperature applications. *Progress in Materials Science*, 118:100769, 2021.

[7] C. Chatelier, Y. Garreau, L. Piccolo, A. Vlad, A. Resta, J. Ledieu, V. Fournée, M.-C. deWeerd, F.-E. Picca, M. deBoissieu, R. Felici, A. Coati, and É. Gaudry. From the Surface Structure to Catalytic Properties of Al_5Co_2(2-10): A Study Combining Experimental and Theoretical Approaches. *J. Phys. Chem. C*, 124:4552–4562, 2020.

[8] H. R. Sharma, K. Nozawa, J. A. Smerdon, P. J. Nugent, I. McLeod, V. R. Dhanak, M. Shimoda, Y. Ishii, A. P. Tsai, and R. McGrath. Templated Three-Dimensional Growth of Quasicrystalline Lead. *Nat. Commun.*, 4:2715, 2013.

[9] V. Fung, G. Hu, P. Ganesh, and B.G. Sumpter. Machine learned features from density of states for accurate adsorption energy prediction. *Nat. Commun.* , 12:88, 2021.

[10] H.-Y. Kwon, Z. Morrow, C. T. Kelley, and E. Jakubikova. Interpolation Methods for Molecular Potential Energy Surface Construction. *J. Phys. Chem. A*, 125:9725–9735, 2021.

[11] J. H. Montoya and K. A. Persson. A high-throughput framework for determining adsorption energies on solid surfaces. *npj Comput. Mater.*, 3:14, 2017.

[12] L. Himanen, P. Rinke, and A. S. Foster. Materials structure genealogy and high-throughput topological classification of surfaces and 2D materials. *npj Comput. Mater.*, 4:1–10, 2018.

[13] K. T. Winther, M. J. Hoffmann, J. R. Boes, O. Mamun, M. Bajdich, and T. Bligaard. Catalysis-Hub.org, an open electronic structure database for surface reactions. *Sci. Data*, 6:75, 2019.

[14] O. Mamun, K. T. Winther, J. R. Boes, and T. Bligaard. High-throughput calculations of catalytic properties of bimetallic alloy surfaces. *Sci Data*, 6:76, 2019.

[15] A.J. Sargood, C. W. Jowett, and B. J. Hopkins. A relationship between surface potentials and electronegativity for adsorption on tungsten single crystals. *Surf. Sci.*, 22:343, 1970.

[16] W. Yang and R. Parr. Hardness, softness, and the fukui function in the electronic theory of metals and catalysis. *Proc. Natl. Acad. Sci.*, 82:6723, 1985.

[17] J. K. Norskov, F. Abild-Pedersen, F. Studt, and T Bligaard. Density functional theory in surface chemistry and catalysis. *Proc. Natl. Acad. Sci.*, 108:937, 2011.

[18] B. Hammer and J. K. Norskov. *Impact of Surface Science on Catalysis*, chapter Theoretical Surface Science and catalysis – Calculations and concepts, pages 71–130. Academic Press, San Diego, 2000.

[19] B. Hammer and J. K. Norskov. Electronic factors determining the reactivity of metal surfaces. *Surf. Sci.*, 343:211, 1995.

[20] A. Vojvodic, J. K. Norskov, and F. Abild-Pedersen. Electronic structure effects in transition metal surface chemistry. *Top. Catal.*, 57:25, 2014.

[21] F. Calle-Vallejo, J. Tymoczko, V. Colic, Q.H. Vu, M.D. Pohl, K. Morgenstern, D. Loffreda, Ph. Sautet, W. Schuhmann W8, and A. Bandarenka. Finding optimal surface sites on heterogeneous catalysts by counting nearest neighbors. *Science*, 350(6257):185–9, 2015.

[22] F. Calle-Vallejo, J. I. Martinez, J. M. Garcia-Lastra, P. Sautet, and D. Loffreda. Fast Prediction of Adsorption Properties for Platinum Nanocatalysts with Generalized Coordination Numbers. *Angew. Chem., Int. Ed.*, 53:8316–8319, 2014.

[23] M. M. Montemore and J. W. Medlin. Scaling relations between adsorption energies for computational screening and design of catalysts. *Catal. Sci. Technol.*, 4:3748–3761, 2014.

[24] F. Abild-Pedersen, J. Greeley, F. Studt, J. Rossmeisl, T. R. Munter, P. G. Moses, E. Skúlason, T. Bligaard, and J. K. Norskov. Scaling properties of adsorption energies for hydrogen-containing molecules on transition-metal surfaces. *Phys. Rev. Letters*, 99:016105, 2007.

[25] A. J. Chowdhury, W. Yang, E. Walker, O. Mamun, A. Heyden, and G. A. Terejanu. Prediction of adsorption energies for chemical species on metalcatalyst surfaces using machine learning. *J. Phys. Chem. C*, 122:28142, 2018.

[26] S. Saini, S. H. Stenlid, and F. Abild-Pedersen. Electronic structure factors and the importance of adsorbate effects in chemisorption on surface alloys. *NPJ Computational Materials*, 163:1, 2022.

[27] J. B. Witkoskie and D. J. Doren. Neural Network Models of Potential Energy Surfaces: Prototypical Examples. *J. Chem. Theory Comput.*, 1:14, 2005.

[28] T. B. Blank, S. D. Brown, A. W. Calhoun, and D. J. Doren. Neural network models of potential energy surfaces. *The Journal of Chemical Physics*, 103:4129, 1995.

[29] J. Behler and M. Parrinello. Generalized neural-network representation of high-dimensional potential-energy surfaces. *Phys. Rev. Lett.*, 98:146401, Apr 2007.

[30] A.P. Bartók, M.C. Payne, R. Kondor, and G. Csányi. Gaussian approximation potentials: The accuracy of quantum mechanics, without the electrons. *Phys. Rev. Lett.*, 104:136403, Apr 2010.

[31] J. Behler. Atom-centered symmetry functions for constructing high-dimensional neural network potentials. *J. Chem. Phys.*, 134:074106, 2011.

[32] H. Jung, L. Sauerland, S. Stocker, K. Reuter, and J.T Margraf. Machine-learning driven global optimization of surface adsorbate geometries. *npj Computational Materials*, 9(1):114, 2023.

[33] M. Andersen, S. Levchenko, M. Scheffler, and K. Reuter. Beyond Scaling Relations for the Description of Catalytic Materials. *ACS Catal.*, 9:2752–2759, 2019.

[34] R. Garcia-Muelas and N. Lopez. Statistical learning goes beyond the d-band model providing the thermochemistry of adsorbates on transition metals. *Nat Commun*, 10:4687, 2019.

[35] R. A. Hoyt, M. M. Montemore, I. Fampiou, W. Chen, G. Tritsaris, and E. Kaxiras. Machine Learning Prediction of H Adsorption Energies on Ag Alloys. *J. Chem. Inf. Model.*, 59:1357–1365, 2019.

[36] K. Tran and Z. W. Ulissi. Active learning across intermetallics to guide discovery of electrocatalysts for co2 reduction and h2 evolution. *Nat. Catal.*, 1:696, 2018.

[37] X. Li, B. Li, Z. Yang, Z. Chen, W. Gao, and Q. Jiang. A transferable machine-learning scheme from pure metals to alloys for predicting adsorption energies. *J. Mater. Chem. A*, 10:872, 2022.

[38] T. Xie and J. C. Grossman. Crystal graph convolutional neural networks for an accurate and interpretable prediction of material properties. *Phys. Rev. Lett.*, 120:145301, 2018.

[39] K. T. Schütt, P.-J. Kindermans, and H. E. Sauceda. Schnet: A continuous-filter convolutional neural network for modeling quantum interactions. Long Beach, CA, USA, 2017.

[40] J. Klicpera, S. Giri, J. T. Margraf, and S. Günnemann. Fast and uncertainty-aware directional message passing for non-equilibrium molecules. 2020.

[41] J. Klicpera, J. Gross, and S. Günnemann. Directional messagepassing for molecular graphs. 2020.

[42] I. Batatia, P. Benner, Y. Chiang, A. M. Elena, D. P. Kovacs, J. Riebesell, X. R. Advincula, M. Asta, M. Avaylon, W. J. Baldwin, F. Berger, N. Bernstein, A. Bhowmik, S. M. Blau, V. Carare, J. P. Darby, S. De, F. Della-Pia, V. L. Deringer, R. Elijosius, Z. El-Machachi, F. Falcioni, E. Fako, A. C. Ferrari, A. Genreith-Schriever, J. George, R. E. A. Goodall, C. Grey, P. Grigorev, S. Han, W. Handley, H. H. Heenen, K. Hermansson, C. Holm, S. Hofmann, J. Jaafar, K. S. Jakob, H. Jung, V. Kapil, A. D. Kaplan, N. Karimitari, J. R. Kermode, N. Kroupa, J. Kullgren, M. C. Kuner, D. Kuryla, G. Liepuoniute, J. T. Margraf, I.-B. Magdau, A. Michaelides, J. H. Moore, A. A. Naik, S. P. Niblett, S. W. Norwood, N. ONeill, C. Ortner, K. A. Persson, K. Reuter, A. S. Rosen, L. L. Schaaf, C. Schran, B. X. Shi, E. Sivonxay, T. K. Stenczel, V. Svahn, C. Sutton, T. D. Swinburne, J. Tilly, C van-der Oord, S. Vargas, E. Varga-Umbrich, T. Vegge, M. Vondrak, Y. Wang, W. C. Witt, F. Zills, and G. Csanyi. A foundation model for atomistic materials chemistry. *arXiv preprint arXiv:2401.00096*, 2024.

[43] A. Jain, S. P. Ong G. Hautier, W. Chen, W. D. Richards, W. Dacek, S. Cholia, D. Gunter, D. Skinner, G. Ceder, and K. A. Persson. Commentary: The Materials Project: A materials genome approach to accelerating materials innovation. *APL Mater.*, 1:011002, 2013.

[44] L. Chanussot, A. Das, S. Goyal, T. Lavril, M. Shuaibi, M. Riviere, K. Tran, J. Heras-Domingo, C. Ho, W. Hu, A. Palizhati, A. Sriram, B. Wood, J. Yoon, D. Parikh, C. L. Zitnick, and Z. Ulissi. Open catalyst 2020 (oc20) dataset and community challenges. *ACS Catal.*, 11:6059, 2021.

[45] T. Szilvasi, B. W. J. Chen, and M. Mavrikakis. Identification of stable adsorption sites and diffusion paths on nanocluster surfaces: an automated scanning algorithm. *npj Comput. Mater.*, 5:101, 2019.

[46] J. Ko, H. Kwon, H. Kang, B.-K. Kimb, and J. W. Han. Universality in surface mixing rule of adsorption strength for small adsorbates on binary transition metal alloys. *Phys. Chem. Chem. Phys.*, 17:3123, 2015.

[47] M. P. Andersson, T. Bligaard, A. Kustov, K. E. Larsen, J. Greeley, T. Johannessen, C. H. Christensen, and J. K. Norskov. Toward computational screening in heterogeneous catalysis: Pareto-optimal methanation catalysts. *J. Catal.*, 239:501, 2006.

[48] M. Meier, J. Ledieu, V. Fournée, and É. Gaudry. Semi-hydrogenation of acetylene on Al_5Co_2 surfaces. *J. Phys. Chem. C*, 121:4958–4969, 2017.

[49] I. Batatia, D. P. Kovacs, G. N. C. Simm, C. Ortner, and G. Csanyi. Mace: Higher order equivariant message passing neural networks for fast and accurate force fields. *arXiv preprint arXiv: arXiv.2206.07697*, 2022.

[50] N. Shoghi, A. Kolluru, J. R. Kitchin, Z. W. Ulissi, C. L. Zitnick, and B. M. Wood. From Molecules to Materials: Pre-training Large Generalizable Models for Atomic Property Prediction.

[51] M. Armbrüster, K. Kovnir, M. Friedrich, D. Teschner, G. Wowsnick, M. Hahne, P. Gille, L. Szentmiklosi, M. Feuerbacher, M. Heggen, F. Girgsdies, D. Rosenthal, R. Schlögl, and Y. Grin. $Al_{13}Fe_4$ as a Low-Cost Alternative for Palladium in Heterogeneous Hydrogenation. *Nat. Mater.*, 11:690–693, 2012.

[52] L. Piccolo, C. Chatelier, M.-C. de Weerd, F. Morfin, J. Ledieu, V. Fournée, P. Gille, and É. Gaudry. Catalytic Properties of $Al_{13}TM_4$ Complex Intermetallics: Influence of the Transition Metal and the Surface Orientation On Butadiene Hydrogenation. *Sci. Tech. Adv. Mater.*, 20:557–567, 2019.

[53] K. Anand, V. Fournée, G. Prévot, J. Ledieu, and É. Gaudry. Non-Wetting Behavior of Al-Co Quasicrystalline Approximants Owing to their Unique Electronic Structures. *Appl. Mater. Inter.*, 12:15793–15801, 2020.

[54] C. Chatelier, K. Anand, P. Gille, M.-C. De Weerd, J. Ledieu, V. Fournée, A. Resta, A. Vlad, Y. Garreau, A. Coati, and E. Gaudry. Revealing the Epitaxial Interface between Al13Fe4 and Al5Fe2 Enabling Atomic Al Interdiffusion. *ACS Appl. Mater. Interfaces*, 15:19593, 2023.

[55] P. Priputen, M. Kusý, M. Drienovský, D. Janičkovič, R. Čička, I. Černičková, and J. Janovec. Experimental Reinvestigation of Al–Co Phase Diagram in Vicinity of $Al_{13}Co_4$ Family of Phases. *J. Alloys Compd.*, 647:486–497, 2015.

[56] P. Simon, I. Zelenina, R. Ramlau, W. Carrillo-Cabrera, U. Burkhardt, H. Borrmann, R. Cardoso-Gil, M. Feuerbacher, P. Gille, and Yu. Grin. Structural complexity of the intermetallic compound o-$Al_{13}Co_4$. *Journal of Alloys and Compounds*, 820:153363, 2020.

[57] J. Grin, U. Burkhardt, M. Ellner, and K. Peters. Crystal Structure of Orthorhombic Co_4Al_{13}. *J. Alloys Compd.*, 206:243–247, 1994.

[58] U. Burkhardt, M. Ellner, Y. Grin, and B. Baumgartner. Powder Diffraction Refinement of the Co_2Al_5 Structure. *Powder Diffr.*, 13:159–162, 1998.

[59] O Bindech, C Goyhenex, and É Gaudry. A tight-binding atomistic approach for point defects and surfaces applied to the o-al13co4 quasicrystalline approximant. *Computational Materials Science*, 200:110826, 2021.

[60] C. Chatelier, Y. Garreau, A. Vlad, J. Ledieu, A. Resta, V. Fournée, M.-C. de Weerd, A. Coati, and E. Gaudry. The pseudo-twofold surface of the $Al_{13}Co_4$ catalyst: structure, stability, and hydrogen adsorption. *ACS Applied Materials & Interfaces*, 12:39787–39797, 2020.

[61] Ph. Scheid, C. Chatelier, J. Ledieu, V. Fournée, and É. Gaudry. Bonding Network and Stability of Clusters: The Case Study of the $Al_{13}TM_4$ Pseudo-10fold Surfaces. *Acta Crystallogr. A*, 75:314–324, 2019.

[62] É. Gaudry, C. Chatelier, G. McGuirk, L. Serkovic Loli, M.-C. DeWeerd, J. Ledieu, V. Fournée, R. Felici, J. Drnec, G. Beutier, and M. de Boissieu. Structure of the $Al_{13}Co_4(100)$ Surface: Combination of Surface X-Ray Diffraction and Ab Initio Calculations. *Phys. Rev. B*, 94:165406, 2016.

[63] J. Ledieu, É. Gaudry, M.-C. de Weerd, R. D. Diehl, and V. Fournée. The (100) surface of the $Al_{13}Co_4$ quasicrystalline approximant. *Mater. Res. Soc. Symp. Proc.*, 1517, 2012.

[64] H. Shin, K. Pussi, É. Gaudry, J. Ledieu, V. Fournée, S. Alarcón-Villaseca, J.-M. Dubois, Yu. Grin, P. Gille, W. Moritz, and R.D. Diehl. Structure of the Orthorhombic $Al_{13}Co_4(100)$ Surface Using LEED, STM and Ab Initio Studies. *Phys. Rev. B*, 84:085411 (1to11), 2011.

[65] J. Hafner. Ab-initio simulations of materials using vasp: Density-functional theory and beyond. *Journal of Computational Chemistry*, 29:2044–2078, 2008.

[66] P. E. Blochl. Projector Augmented-Wave Method. *Phys. Rev. B*, 50:17953–17979, 1994.

[67] M. Mihalkovič and M. Widom. First-Principles Calculations of Cohesive Energies In the Al-Co Binary Alloy System. *Phys. Rev. B*, 75:014207, 2007.

[68] D. Kandaskalov, V. Fournée, J. Ledieu, and É. Gaudry. Catalytic Semihydrogenation of Acetylene on the (100) Surface of the o-$Al_{13}Co_4$ Quasicrystalline Approximant: Density Functional Theory Study. *J. Phys. Chem. C*, 121:18738–18745, 2017.

[69] J. P. Perdew, K. Burke, and M. Ernzerhof. Generalized Gradient Approximation Made Simple . *Phys. Rev. Lett.*, 77:3865, 1996.

[70] S. Grimme, S. Ehrlich, and L. Goerigk. Effect of The Damping Function in Dispersion Corrected Density Functional Theory. *J. Comput. Chem.*, 32:1456, 2011.

[71] H.J. Monkhorst and J.D. Pack. Special points for Brillouin-zone integrations. *Phys. Rev. B*, 13:5188–5192, 1976.

[72] É. Gaudry, C. Chatelier, D. Loffreda, D. Kandaskalov, A. Coati, and L. Piccolo. Catalytic activation of a non-noble intermetallic surface through nanostructuration under hydrogenation conditions revealed by atomistic thermodynamics. *J. Mater. Chem. A*, 8:7422–7431, 2020.

[73] F. Brix and E. Gaudry. Two-dimensional metal structures revealed by evolutionary computations: Pb/Al13Co4(100) as a case study. *J. Vac. Sci. Technol. A*, 40:012203, 2022.

[74] A. P. Bartok, R. Kondor, and Gabor G. Csanyi. On representing chemical environments. *Phys. Rev. B*, 87:184115, 2013.

[75] L. Himanen, , M. Jäger, E. V. Morooka, F. F. Canova, Y. S. Ranawat, D. Z. Gao, P. Rinke, and A. S. Foster. DScribe: Library of descriptors for machine learning in materials science. *Computer Physics Communications*, 247:106949, 2020.

[76] Davide Mandelli, Barak Hirshberg, and Michele Parrinello. Metadynamics of paths. *Phys. Rev. Lett.*, 125:026001, Jul 2020.

[77] M. O. J. Jäger, E. V. Morooka, F. Canova, L. Himanen, and A. S. Foster. Machine learning hydrogen adsorption on nanoclusters through structural descriptors. *npj Comput. Mater.*, 4:37, 2018.

[78] Albert P Bartók, Sandip De, Carl Poelking, Noam Bernstein, James R Kermode, Gábor Csányi, and Michele Ceriotti. Machine learning unifies the modeling of materials and molecules. *Science advances*, 3(12):e1701816, 2017.

[79] C.E. Rasmussen. *Advanced Lectures on Machine Learning, Lecture Notes in Computer Science, vol 3176*, chapter Gaussian Processes in Machine Learning. Springer, Berlin, Heidelberg, 2004.

[80] T. Lewis-Atwell, P.A. Townsend, and M. N. Grayson. Machine learning activation energies of chemical reactions. *WIREs Comput Mol Sci.*, 12:e1593, 2022.

[81] D. Kandaskalov, V. Fournée, J. Ledieu, and É. Gaudry. Adsorption properties of the o-$Al_{13}Co_4$(100) surface towards molecules involved in the semi-hydrogenation of acetylene. *J. Phys. Chem. C*, 118:23032–2304, 2014.

[82] J. Jacobsen, SB. Hammer, K.W. Jacobsen, and J.K. Norskov. Electronic structure, total energies, and STM images of clean and oxygen-covered Al(111). *Phys. Rev. B*, 52:14954, 1995.

[83] S. Alarcon-Villaseca, J.-M. Dubois, and E. Gaudry. Lead adsorption on the pseudo-10-fold surface of the Al13Co4 complex metallic alloy: A first principle study. *International Journal of Quantum Chemistry*, 113:840–846, 2013.

[84] W. Malone and A. Kara. Predicting adsorption energies and the physical properties of h, n, and o adsorbed on transition metal surfaces: A machine learning study. *Surface Science*, 731:122252, 2023.

[85] T.W. Ko, J. A. Finkler, S. Goedecker, and J. Behler. A fourth-generation high-dimensional neural network potential with accurate electrostatics including non-local charge transfer. *Nature Communications*, 398:1, 2021.

[86] Z. Li and S. Wang and W.S. Chin and L.E. Achenie and H. Xin. High-throughput screening of bimetallic catalysts enabled by Machine Learning. *J. Mater. Chem. A.*, 5:24131, 2017.

[87] S. Back, J. Yoon, N. Tian, W. Zhong, K. Tran, and Z.W. Ulissi. Convolutional neural network of atomic surface structures to predict binding energies for high-throughput screening of catalysts. *J. Phys. Chem. Lett.*, 10:4401, 2019.

[88] G.H. Gu, J. Noh, S. Kim, S. Back, Z. Ulissi, and Y. Jung. Practical deep-learning representation for fast heterogeneous catalyst screening. *J. Phys. Chem. Lett.*, 11:3185, 2020.

[89] R. Kronberg, H. Lappalainen, and K. Laasonen. Hydrogen adsorption on defective nitrogen-doped carbon nanotubes explained via machine learning augmented dft calculations and game-theoretic feature attributions. *The Journal of Physical Chemistry C*, 125(29):15918–15933, 2021.

[90] M. O.J. Jäger, Y. S Ranawat, F. F. Canova, E.V. Morooka, and A.S. Foster. Efficient machine-learning-aided screening of hydrogen adsorption on bimetallic nanoclusters. *ACS combinatorial science*, 22(12):768–781, 2020.

[91] A. Montoya, A. Schlunke, and B. S. Haynes. Reaction of Hydrogen with Ag(111): Binding States, Minimum Energy Paths, and Kinetics. *J. Phys. Chem. B*, 110:17145, 2006.